(U)

SECURITY CLASSIFICATION OF THIS PAGE

REPORT DOCUMENTATION PAGE

Form Approved
OMB No. 0704-0188

1a. REPORT SECURITY CLASSIFICATION UNCLASSIFIED	1b. RESTRICTIVE MARKINGS
2a. SECURITY CLASSIFICATION AUTHORITY	3. DISTRIBUTION / AVAILABILITY OF REPORT DISTRIBUTION IS UNLIMITED
2b. DECLASSIFICATION / DOWNGRADING SCHEDULE	
4. PERFORMING ORGANIZATION REPORT NUMBER(S)	5. MONITORING ORGANIZATION REPORT NUMBER(S) AFOSR-TR-96-0004
6a. NAME OF PERFORMING ORGANIZATION UNIVERSITY OF HOUSTON 6b. OFFICE SYMBOL (If applicable)	7a. NAME OF MONITORING ORGANIZATION AIRFORCE OFFICE OF SCIENTIFIC RESEARCH
6c. ADDRESS (City, State, and ZIP Code) 4800 CALHOUN BLVD. DEPT. OF MECH. ENGR. HOUSTON, TX 77204-4792	7b. ADDRESS (City, State, and ZIP Code) 110 DUNCAN AVE, SUITE B115 BOLLING AFB, DC 20332-0080
8a. NAME OF FUNDING / SPONSORING ORGANIZATION AFOSR 8b. OFFICE SYMBOL (If applicable) NA	9. PROCUREMENT INSTRUMENT IDENTIFICATION NUMBER Grant # F49620-94-1-0403
8c. ADDRESS (City, State, and ZIP Code) 110 DUNCAN AVE, SUITE B115 BOLLING AFB DC 20332-0080	10. SOURCE OF FUNDING NUMBERS PROGRAM ELEMENT NO. 61102F PROJECT NO. 2303 TASK NO. BS WORK UNIT ACCESSION NO.

11. TITLE (Include Security Classification)
Nondestructive Measurement of Impact Toughness of Aircraft Windhsields (U)

12. PERSONAL AUTHOR(S)
K. RAVI-CHANDAR

13a. TYPE OF REPORT	13b. TIME COVERED	14. DATE OF REPORT (Year, Month, Day)	15. PAGE COUNT
FINAL	FROM 7/15/94 TO 10/15/95	1995/12/15	37

16. SUPPLEMENTARY NOTATION

17. COSATI CODES			18. SUBJECT TERMS (Continue on reverse if necessary and identify by block number)
FIELD	GROUP	SUB-GROUP	Impact Toughness, Windshields, Dynamic Fracture

19. ABSTRACT (Continue on reverse if necessary and identify by block number)

This report summarizes the results on the project obtained over the past fifteen months. With a view toward establishing a nondestructive procedure for evaluation of the impact properties of polycarbonate windshield material, we have set up the following experiments (i) a split-Hopkinson bar apparatus for impact strength measurement, (ii) an instrumented impact tester for impact toughness measurement and (iii) a monochromator with a birefringence measuring Babinet-Soleil compensator for optical characterization. Some polycarbonate specimens have been identified as potential candidates for evaluation of the proposed method. A dynamic crack growth model based on an extension of the Dugdale-Barenblatt has been formulated and solved through a finite difference scheme. This model exhibits many of the features observed in dynamic fracture experiments.

20. DISTRIBUTION / AVAILABILITY OF ABSTRACT ☒ UNCLASSIFIED/UNLIMITED ☐ SAME AS RPT. ☑ DTIC USERS	21. ABSTRACT SECURITY CLASSIFICATION UNCLASSIFIED
22a. NAME OF RESPONSIBLE INDIVIDUAL Dr. Walter F. Jones	22b. TELEPHONE (Include Area Code) (202) 767-0470 22c. OFFICE SYMBOL NA

DD Form 1473, JUN 86 Previous editions are obsolete. SECURITY CLASSIFICATION OF THIS PAGE

(U)

NONDESTRUCTIVE MEASUREMENT

OF IMPACT TOUGHNESS OF AIRCRAFT WINDSHIELDS

Final Technical Report to

The Air Force Office of Scientific Research

December 15, 1995

K. Ravi-Chandar

Grant Number F49620-94-1-0403

Department of Mechanical Engineering
UNIVERSITY OF HOUSTON
HOUSTON, TX 77204

1. INTRODUCTION

Aircraft canopies have recently been reclassified as primary structures and much analysis and care has gone into their design as a result of their function as an important component in providing protection to the crew from bird strike (West, 1984). During high-speed, low-altitude flight, encounters with birds can result in severe impact loading to the canopy or windshield. The design against failure during this encounter is based on a characterization of the canopy material in the virgin state; the inelastic deformation capability and the impact fracture toughness are determined at the time of manufacture. However, as a function of time the properties change due to a number of reasons. First, the glassy state of the polymer is a metastable state which slowly evolves towards the equilibrium state; this is termed physical aging and could be modeled using the free volume theories of viscoelasticity. Second, polymers undergo a degradation due to the environment; the driving force for this degradation might be chemical, mechanical, hygroscopic, electromagnetic (for example, photodegradation by UV radiation[1]) etc. The degradation is primarily in terms of changes introduced in the molecular weight; this leads to a long term embrittlement of the material. Very few studies are available on the effect of photodegradation on the mechanical behavior of polycarbonate, but sufficient to indicate that the impact toughness (characterized by a Charpy test) depends on the time of exposure (which controls the molecular weight-determined desctructively through chromatography, Davis and Sims, 1983). Empirical correlations also exist in the literature between molecular weight and strength which lends support to the above correlation between photodegradation of impact toughness and molecular weight. The present work is an attempt at the characterization of the photo-induced changes in the molecualr weight through a non-destructive optical method.

The main idea in the present work is that evaluating the molecular weight and perhaps other attributes of the structure could result in a determination of the toughness of the degraded material. However, we are interested in a nondestructive evaluation; this restricts the type of techniques that are available for polymer characterization. Only inverse techniques based on interrogation of the material with some radiation and interpreting the reflected, refracted or scattered beam would be available; even in this range of techniques, the thickness of the canopy material precludes the use of infrared wavelengths and x-rays due to the poor penetration

[1] Additives are used in the polymers to stabilize against photodegradation by UV.

depth. Wavelengths in the visual range and acoustic disturbances (ultrasonic wave propagation) remain as potential techniques for characterization of molecular structure. Here, we discuss the optical approach. The molecular structure is also related to the optical properties of the material; there exist both theoretical formulations (Lorentz-Lorenz equation) and empirical formulations (Gladstone and Dale, Vogel) (see Van Krevelen, 1990). Optical properties such as reflectance, transmittance, scattering, birefringence, absorption, Raman spectroscopy etc have all been used in the characterization of microstructure. The most promising optical technique relevant to the present problem appears to be the measurement of birefringence and relating it to the microstructure. Treloar (1929) discusses the origin of birefringence in long chain molecules, based on the model of Kuhn and Grün. The optical properties of a single long-chain molecule is modeled based on a chain of equal, randomly jointed links. The chain birefringence has to be again statistically averaged to give the bulk birefringence, assuming that the polymer contains N chains per unit volume. The chain end-to-end distance r is assumed to be equal in all chains, but distributed randomly in orientation. This, however, would lead to a zero birefringence condition[2]. On deforming the material, the chain end-to-end distances do not remain the same, but change in accordance with the imposed stretches, resulting in birefringence. If this birefringence can be measured experimentally, it can then be interpreted in terms of the molecular structure. Using this and the experimentally obtained correlation between the molecular weight and toughness, it should be possible to correlate the birefringence measurements to the changes in the impact toughness due to physical aging or photodegradation.

Of course, experiments are crucial to the validation of this idea. We have set up three different apparatus to examine the correlation between the birefringence and the impact properties of polycarbonate through a series of experiments. In these experiments, commercially obtained GE Lexan polycarbonate of four different grades were used in preparing the specimens. In addition, specimens recovered from some old windshields discarded from service were obtained as an example of weathered (and/or aged) material[3]. From these measurements, based on the

---

[2] Orientation introduced in the material during manufacturing processes such as in injection molding or forming, could lead to a residual birefringence.

[3] Note that since our current aim is not to develop the kinetics of the aging/weathering but to develop a nondestructive toughness measurement scheme, it is not necessary to generate carefully weathered specimens (under known doses of radiation), but only to know the molecular weight, impact toughness and the birefringence; the latter quantities will be measured experimentally. The

discussion above, two correlations can be expected. The first correlation to be established is between impact toughness, K_{Id}, and molecular weight, M_w. The second correlation is between birefringence and molecular weight, guided by the theoretical development of Kuhn and Grün. Using these two correlations, it is then possible to relate the birefringence to impact toughness; this can be verified by first determining birefringence nondestructively, predicting the impact toughness through the empirically established correlation and then performing destructive measurements to determine the actual value. This serves both as a validation exercise and establishes the sensitivity and reliability paramters for the correlation.
In this report, we discuss the three different measurement schemes that were developed to determine the impact strength, impact toughness and the optical characteristics such as spectral transmittance and birefringence.

2. THE SPLIT HOPKINSON BAR - Measurement of Impact Strength

The most widely used means for evaluating the high strain rate behavior of materials is the Split Hopkinson Pressure Bar (SHPB). In brief, the SHPB consists of two long elastic high strength steel bars which sandwich the specimen between them. A striker bar, commonly manufactured from the same material as the pressure bars and accelerated by a gas gun, is propelled towards the free end of one of the bars which is therefore given the name "input bar". In our SHPB set-up, the speed of the projectile can range from about 5 m/s to about 80 m/s. The longitudinal elastic compression wave generated by the impact travels down the bar and is partly reflected and partly transmitted at the input bar/specimen interface. The transmitted wave travels through the specimen and then enters the "output bar". Strain gages are cemented in pairs diametrically apart on the bars so as to cancel any recording of bending waves. Strain gage pairs at A and C measure the longitudinal straining in the axial direction in both the input and output bars, whereas the gage pair at B records the circumferential strain in the input bar and allows measurement of the Poisson's ratio of the bar material. The strain gages are connected to a standard Wheatstone bridge circuit and amplifier. The circuitry was calibrated using a simple tensile test. A schematic diagram of the SHPB setup is displayed in Figure 1. This SHPB apparatus was designed, fabricated and tested as part of this project.

assistance of Dr. Mike Gran at the Flight Dynamics Laboratory at Wright Patterson AFB in obtaining these specimens is gratefully acknowledged.

Traditionally SHPB data analysis is based on one-dimensional elastic wave propagation in the input and output bars. Wave propagation in the specimen is not analyzed; stress equilibrium within the specimen is assumed to be maintained at all times. Let $V_1(t)$ and $V_2(t)$ be the velocities at the input bar/specimen and specimen/output bar interfaces. Let L be the specimen length. The strain rate in the specimen undergoing plastic deformation is given by

$$\dot{\varepsilon} = \frac{V_1(t) - V_2(t)}{L}. \tag{1}$$

Since the two bars deform elastically, the velocities at the interfaces can be expressed in terms of the strains measured by the strain gages as:

$$\begin{aligned} V_1(t) &= C_0(\varepsilon_I - \varepsilon_R) \\ V_2(t) &= C_0\varepsilon_T \end{aligned} \tag{2}$$

where C_0 is the bar wave speed, ε_I, ε_R, and ε_T are the incident, reflected and transmitted strain pulses respectively. The strain can then be found by integrating Eq.(1) as

$$\varepsilon(t) = \frac{C_0}{L}\int_0^t [\varepsilon_I(t) - \varepsilon_R(t) - \varepsilon_T(t)]dt. \tag{3}$$

If it is assumed that the specimen is under equilibrium, we get $\varepsilon_I + \varepsilon_R = \varepsilon_T$ and hence the stress in the bar is given by

$$\sigma(t) = E_0 \frac{A_{bar}}{A_{specomen}} \varepsilon_T(t). \tag{4}$$

It is important to reiterate the assumptions involved in the above analysis: wave propagation in the specimen is not taken into consideration and equilibrium conditions are assumed to be established in the specimen.

Typical strain gage signal traces from a polycarbonate specimen are shown in Figure 2. The transmitted pulse is considerably elongated, being about 2.5 times longer than the incident pulse, as can be seen in Figure 2; an extensive literature review revealed only two papers referring to this phenomenon in polymers. The "dispersion" of the transmitted pulse, however, indicates that the analysis of the SHPB results for polycarbonate needs to be reexamined, including the wave

propagation in the bar. Our first attempt at examining this problem is a simple extension of the Taylor-von Karman analysis. Consider a nonlinear material described by the constitutive behavior

$$\sigma = f(\varepsilon). \tag{5}$$

One dimensional wave propagation in the specimen is then described by

$$\frac{\partial^2 u}{\partial t^2} = \frac{f'(\varepsilon)}{\rho}\frac{\partial^2 u}{\partial x^2}. \tag{6}$$

In the SHPB experiment, the measued strains in the input and output bars enable the determination of the velocities at the specimen-bar interfaces through Eqs.(2), which are then the boundary conditions on the specimen. Thus, if one assumes a form of the constitutive behavior (for instance a power law form), Eq.(6) can be solved numerically (iteratively in some least-square sense) to obtain the parameters of the constitutive law. This is currently under investigation. The result will be a complete characterization of the impact stress-strain behavior of the materials.

3. INSTRUMENTED IMPACT TESTER - Measurement of Impact Toughness

An instrumented impact tower was constructed for measurement of impact fracture toughness in polycarbonate. A sketch of this system is shown in Figure 3. The loading tup is guided by a monorail, nearly 2.5 m long. This results in an impact velocity of about 5 m/s; note that by appropriate specimen design, the specimen can be made to fail within the first wave pass from the tup to the specimen. The loading tup is raised by a hand-cranked winch and held in place by an electromagnetic holder which also serves to initiate the drop experiment. A shock absorber mounted on the base plate stops the tup after impact. The tup is instrumented with a Dytran Model #105V5 piezoelectric force transducer and a Model # 3200B5 piezoelectric accelerometer to determine the contact force and the tup acceleration. The transducer outputs were recorded on an Tektronix Model TDS 460 digital sampling oscilloscope and then transferred to a personal computer through a GPIB bus for later data interpretation and analysis. The loading tup and the specimen support rollers have a 1/4" radius. The specimen itself is a three point bend configuration, with a crack machined in the middle; the span can vary in the range of 2 to 10 inches. The instrumented impact tester was designed such that it can be placed in the field of view of a high speed camera in order to examine the crack initiation and growth

using high speed photography; the design also allows for the incorporation of an environmental chamber to control the specimen temperature.

Our initial expectation was that the accelerometer data might be integrated to obtain tup displacement, this turned out to be difficult due to the noise and ringing of several components of the tup. Thus, the output from the accelerometer was used as only as the trigger for the entire system. The output from the force transducer from four impact experiments are shown in Figure 4. All the specimens had a span of 8 inches and a height of 4 inches. The specimen thickness was nominally 0.25 inches. The initial crack length in each of the tests was varied and is indicated in Figure 4; the ligament length is the specimen height minus the crack length. For the first 200 μs, all specimens behave identically; crack initiation occurs at the time indicated by the arrow. At longer times, for the specimens with a shorter initial crack, beam oscillation mode is apparent. The impact fracture toughness or fracture energy can be calculated simply from this data. We also have the possibility for examining the loading and crack growth using a high speed camera and this work will continue.

4. MONOCHROMATOR - Measurement of optical properties

A monochromator system was assembled to examine the optical properties of the polycarbonate. The system consists of a 1/4 mm grating monochromator, polarizers, a Babinet-Soleil compensator and a photodetector. The system is capable of measuring transmittance as well as birefringence over a wavelength range from about 300 nm to about 900 nm, thus spanning the range from near ultraviolet to near infrared wavelengths. Figure 5 shows a block diagram of this apparatus. So far we have examined the spectral transmittance of polycarbonate and the results are described below.

The light source is a filament lamp and thus has a sharp spectral output which needs to be calibrated. Figure 6 shows the spectral response of the system in the absence of any specimen. Note that this provides a combined response of both the light source and the photodetector; a separate calibration of each is not necessary. Eventhough the light source exhibits a strong peak at around 660 nm, the signal is quite strong and stable in the complete range from about 300 nm to about 900 nm. This is the range of wavelengths in which the behavior of polycarbonate will be examined. Figure 7 shows the transmittance of six different grades of polycarbonate. Two of these are commercial grade sheets of GE Lexan, one clear and the other one

tinted. One sheet was obtained from a fusion bonded windshield material recovered from service. The other three samples were fabricated from pellets supplied by GE[4]. All the samples except the tinted grade behave in a similar manner in the wavelength range from about 450 nm to about 900 nm with a transmittance of about 90%; the tinted sample absorbs almost 50% of the incident light. The main differences are seen in the range from about 300 nm to about 450nm. The commerical grades and the windshield material are made with ultraviolet stabilizers that absorb UV; clearly a sharp cut off in the transmittance is seen for wavelengths less than about 400 nm. The samples made from the pellets were not incorporated with a UV stabilizer and hence their transmittance in the range from about 340 nm to 400 nm is significantly higher. Thus, we expect to be able to degrade these samples over time with exposure to UV and then examine their strength and toughness property variations with time.

5. MODELING OF DYNAMIC FRACTURE

In parallel to our efforts at examining impact behavior experimentally, especially since the fabrication of the three systems described above and specimen delivery took time, we devoted some attention towards generating a model for dynamic crack growth. The background of the model and some results are described below.

Dynamic fracture in nominally brittle materials has been shown to occur through the nucleation, growth, interaction and coalescence of microcracks (Ravi-Chandar and Knauss, 1984a-d, Ravi-Chandar and Yang, 1995) These studies have suggested that the fracture process zone which accompanies a dynamically propagating crack plays a crucial role in determining the dynamics of crack growth including the limiting crack speed and branching. However, in theoretical and numerical modeling of dynamic fracture, the influence of the microcrack interaction in the fracture process zone is seldom taken into account, primarily due to the difficulty in handling the microcrack interaction problems. Johnson (1992) has attempted a numerical simulation in which the microcrack damaged near tip region is modeled by a damage mechanics model; while the computational effort associated with this model is expensive, this model appears to present a dynamic fracture behavior similar to that observed experimentally. More recently, Xu and Needleman (1994) examined using finite element modeling, dynamic crack branching problems with a

[4]These Lexan grades 101, 121 and 142 were supplied by GE as pellets. We acknowledge the support of Dr. Vijay Stokes in supplying this material.

force separation law to model damage generation; once again the computational effort is expensive. Furthermore, for crack branching type problems, the geometry of the mesh (triangular vs rectangular) produces a significant influence on the crack path.

In theoretical models of dynamic fracture, the governing field equations and the failure criterion are usually decoupled and two strategies are used in combining the them during post-processing. The first strategy is to use the crack growth history observed in an experiment to perform the theoretical or numerical analysis (called the generation phase) and to use the results to extract the dynamic fracture criterion. The second strategy is to find dynamically admissible fields from the governing equations of elastodynamics for an arbitrary, constant crack speed and then to pick out the appropriate crack speed by imposing the failure criterion; this is called the application phase. In either of these two approaches, one usually relies on the applicability of the dynamic stress intensity factor as the appropriate parameter characterizing fracture. Certain assumptions are inherent in this approach to dynamic fracture modeling. First, it is assumed that any experimental configuration can be used in the generation phase of the analysis to determine the dynamic crack growth criterion. The dynamic crack growth criterion has been usually characterized as a relationship between the instantaneous stress intensity factor, K, and the instantaneous crack speed, v, which is determined through experiments; there has been quite an intense debate about the validity of such a characterization; Kalthoff (1983) and Kobayashi and Mall (1978) found that the K-v characterization was dependent on the specimen geometry while Ravi-Chandar and Knauss (1984c) indicated that the K-v characterization is non-unique since it is history dependent. Second, in the applications phase, it is assumed that a K-v characterization obtained from a set of experiments can be used to predict non-steady crack propagation by successive smooth transitions through the steady state results. We will examine both these assumptions in this paper.

A number of other crack growth models have been proposed over the last three decades aimed at explaining the experimental observations of dynamic brittle fracture. Most of these models are derived from an idealized brittle crack model (Freund, 1990) and do not include a fracture process zone. Although some models have incorporated plasticity through a Dugdale type cohesive zone or an elastic-plastic constitutive law, the analyses have usually imposed the crack velocity as an

external parameter, assumed to be known. Models incorporating variations in the fracture resistance of the material have also been considered in a similar setting. To date, however, none of these models (other than the damage models) have been able to generate all the experimentally observed features. In particular, the experimental observation of a limiting crack speed that is smaller than the Rayleigh wave speed is not predicted by the models; also, periodicity in the roughness of the fracture surface and crack branching have eluded analytical description. In this paper we begin with a formulation of the dynamic fracture problem that is fully coupled; the fracture criterion is imposed along with the governing field equations and the initial-boundary conditions. In an effort to model the actual nucleation, growth and breakdown of a fracture process zone which develops even in nominally brittle materials, a cohesive zone model is imposed in a layer ahead of the crack tip. This is similar to the usual Dugdale-Barenblatt model applied to the dynamic crack problem. In this model, crack growth occurs naturally as a result of breakdown of the fracture process zone governed by the rate at which energy flows into the crack tip process zone.

5.1 Formulation of an Anti-Plane Fracture Problem

5.1.1 Ideal Brittle Fracture

Consider an edge crack of length l in a half space, as shown in Figure 8. The material is initially stress free and at rest. The two-dimensional anti-plane motions of the homogeneous, isotropic, linear elastic body is completely determined by the out-of-plane displacement, $w(x,y,t)$ which satisfies the wave equation

$$\frac{\partial^2 w}{\partial x^2}+\frac{\partial^2 w}{\partial y^2}=\frac{1}{c_2^2}\frac{\partial^2 w}{\partial t^2}. \tag{7}$$

Here c_2 is the shear wave speed given by $c_2=\sqrt{k_1/\rho}$, k_1 is the shear modulus of the bulk material and ρ is the density. At $t = 0$, boundary displacements on $x = 0$ are applied corresponding to anti-plane shear displacements:

$$w(0,y,t)=w_0 f(t) \quad for \quad y>0, \tag{8}$$

where $f(t)$ is a prescribed function. The crack faces are considered to be traction free:

$$\sigma_{32}(x,0^+,t)=0 \quad for \quad 0<x<l(t), \tag{9}$$

where $l(t)$ is the time variation of the crack tip position, to be determined as part of the solution to the problem. In the traditional formulation of this problem, the anti-plane symmetry is imposed by applying

$$w(x,0^+,t)=0 \quad for \quad x>l(t). \tag{10}$$

To complete the formulation of the anti-plane shear problem, one must now specify an evolution equation that governs $l(t)$. In the spirit of Griffith's equilibrium crack formulation, the governing equation determining the evolution of the crack position is given by the global energy rate balance equation

$$(-\dot{W}+\dot{U}+\dot{K})+\dot{D}=0 \tag{11}$$

where $\dot{W}$ is the rate of external work, $\dot{U}$ is the rate of change of strain energy, $\dot{K}$ is the rate of change of kinetic energy and $\dot{D}$ is the rate of dissipation at the crack tip. Equivalently, a local version of the energy rate balance can be obtained (Freund, 1990). The energy flux into the crack tip region is given by

$$F(\Gamma)=\int_{\Gamma}\left[\sigma_{ij}n_j\frac{\partial u_i}{\partial t}+(U+T)vn_1\right]ds, \tag{12}$$

where Γ is a contour moving along with the crack tip at its instantaneous speed v as shown in Figure 9 and n_i are the components of the unit outward normal to the contour. It is assumed here the crack moves along the line $y = 0$. Note that the energy flux integral is not path independent except in the case of steady-state crack motion defined by a constant crack speed. The fracture criterion is given by

$$F(\Gamma) = \dot{D}. \tag{13}$$

Equations (7) through (10) together with (13) represent the complete formulation of the dynamic crack problem in anti-plane shear. The solution to this problem has not been found in this generality; as remarked earlier, the usual strategy for solving dynamic fracture problems is to obtain the dynamically admissible stress and displacement fields from the governing equation (7) subjected to the conditions (8) through (10) under an assumed steady state crack speed v and then to use the energy rate balance equation (13) as the crack tip equation of motion to determine the crack speed.

An asymptotic analysis of the governing equation (7) for arbitrary crack speed produces a singular stress field near the crack tip which is physically unrealistic. Typically, for a brittle fracture, a negligibly small fracture process zone is considered to alleviate this problem, but the details of the fracture process zone are not usually fully analyzed. In other words, the singular stress field is assumed to govern the evolution of the crack motion. From the asymptotic analysis, the Cartesian components of the crack tip stress field can be expressed in terms of a single parameter, the mode III stress intensity factor, $K_{III}(t)$ as follows:

$$\begin{Bmatrix} \sigma_{31}(r,\theta,t) \\ \sigma_{32}(r,\theta,t) \end{Bmatrix} = \frac{K_{III}(t)}{\sqrt{2\pi r}} \begin{Bmatrix} -\dfrac{\sin\dfrac{\theta_s}{2}}{\alpha_s\sqrt{\gamma_s}} \\ \dfrac{\cos\dfrac{\theta_s}{2}}{\sqrt{\gamma_s}} \end{Bmatrix} \quad \text{for} \quad r \to 0 \tag{14}$$

where $\alpha_s = \sqrt{1-(v/c_s)^2}$, $\gamma_s = \sqrt{1-(v\sin\theta/c_s)^2}$ and $\theta_s = \arctan(\alpha_s \tan\theta)$. The energy flux integral in (12) can be evaluated along a contour lying in the region where the crack tip stress field is given by (14) and expressed in terms of the stress intensity factor as

$$F(\Gamma) = \frac{K_{III}^2(t)v}{2k_1\alpha_s}. \tag{15}$$

Also, for a brittle fracture, the dissipation is considered to be rate independent and thus one obtains $\dot{D} = \Gamma_s v$, where Γ_s is the surface energy per unit crack area. Now the equation of crack motion becomes

$$\frac{K_{III}^2(t)}{2k_1\sqrt{1-(v/c_s)^2}} = \Gamma_s. \tag{16}$$

This is the basis of the K-v curve that is commonly used to characterize dynamic crack growth criterion. A parallel development is used to formulate the in-plane problems under plane strain or plane stress, but we will restrict attention in this paper to the mode III anti-plane shear problem.

Other anti-plane problems have been investigated by Kostrov, (1966), Achenbach and Dunayevsky (1982), Freund (1990) among others. Inelastic material behavior has

been incorporated in some of the investigations: Freund (1990), Slepyan (1976), Freund and Douglas (1982) and others. It is not our intent to review this development in detail. For our purpose, it is sufficient to note that in all of these analyses, the fracture criterion is decoupled from the field problem just as in the case of the elasticity problem discussed above. The goal of the present investigation is to examine the fully coupled dynamic fracture problem. In other words, by solving the governing equations along with the boundary conditions and the fracture criterion, the crack extension behavior is obtained from the solution rather than being imposed, without any post processing for imposition of the energy balance equation. Of course, the nature of the fracture criterion plays a key role in the solution procedure; we begin with a very simple model that takes off from a cohesive zone description.

5.1.2 Cohesive Zone Model of Fracture

In an effort to model the nucleation, growth and breakdown of a crack tip process zone, the material behavior on the line ahead of the crack tip is assumed to be of the elastic-softening type, with a peak load. This is equivalent to assuming that a thin adhesive layer exists, joining two elastic plates. This idea is derived from the Dugdale-Barenblatt model for the crack tip and similar modeling of a cohesive zone has been used in quasi-static problems by Anderson, (1969), Ungsuwarangsri and Knauss, (1987), and Carpinteri, (1994) among others. It is initially assumed that the layer is of uniform thickness and that the crack proceeds in the middle plane of the layer. This is a severe restriction which needs to be examined further, particularly since it is known that the process zone thickness changes dramatically (Ravi-Chandar and Knauss, 1984b, Fineberg *et al.*, 1991, Ravi-Chandar and Yang, 1995). In fact, the variation in the process zone size is considered to be the main cause of the lower limiting speed, crack surface oscillations and crack branching. In nominally brittle materials, this layer can be considered to be the damage zone developed by the enhanced stress field near the crack tip, through microcrack nucleation, growth and coalescence. In this sense, in order to apply the model developed here to such materials, a constitutive characterization relating the stress strain behavior of the layer to the microcracking behavior (incorporating the dynamic behavior as necessary) would have to be developed. For the present purposes, we shall simply assume the constitutive behavior of the layer and examine its consequences on dynamic crack growth. A representative idealized constitutive law of the layer material is shown schematically in Figure 10. The material behaves linear elastically,

with the same modulus as the bulk material until reaching a critical strain γ_y. After the peak-load corresponding to this strain level, the material gets damaged progressively such that with increasing strain, the stress drops linearly to zero at γ_f, indicating a separation of the layer material at this strain level. Unloading is modeled by the secant line at any strain level, thus imposing irreversibility of the partially damaged state of the layer. Thus the layer behavior under monotonically increasing loading is defined by

$$\tau_{layer} = \begin{cases} k_1 \gamma_{layer} & 0 < \gamma_{layer} < \gamma_y \\ k_1 \gamma_y - k_2 \left(\gamma_{layer} - \gamma_y \right) & \text{for } \gamma_y < \gamma_{layer} < \gamma_f \\ 0 & \gamma_{layer} > \gamma_f \end{cases} . \tag{17}$$

The deformation of the layer is assumed to be uniform in the z-direction. Thus the shear strain in the layer is $\gamma_{layer} = w(x,0,t)/d$, where d is half of the thickness of the layer. Now the complete anti-plane problem is to find $w(x,y,t)$ that satisfies equations (7) through (9) and the layer constitutive behavior given in equation (17). The evolution equation for $l(t)$ is contained in (17). Note that the constitutive law for the layer is such that the singularity of the linear elastic problem is eliminated. Instead, the crack tip stress is limited to a maximum value $k_1 \gamma_y$, and a fracture process zone develops near the crack tip. Furthermore, the constitutive behavior of the layer is independent of the rate of loading; the energy dissipated per unit extension of the crack extension is simply the area under the stress-strain curve up to γ_f. and we shall refer to this as Γ_s. This cohesive zone model of the dynamic fracture problem is solved using a finite-difference scheme as discussed in the next section.

5.2 Finite Difference Scheme

We adopt the finite difference scheme to find numerical solutions to the cohesive zone model of the dynamic fracture problem. The region $x \geq 0,\ y \geq 0$, is discretized into a rectangular grid with a uniform mesh size in both the x and y directions: $\Delta x = \Delta y = h$. The mesh size, h, is dictated by our desire to have at least 10 nodes within the cohesive zone when it develops. The nodes are at

$$\left(x(I), y(J)\right) = (Ih, Jh) \qquad I, J = 0,1,2,.... \tag{18}$$

The time increment is taken to be Δt, whose magnitude is to be determined based on numerical stability considerations. The Courant-Freidrich-Lewy stability criterion requires that

$$\frac{c_2 \Delta t}{h} \leq 1 \tag{19}$$

and in our calculations this was maintained at 0.7. The displacement $w(x,y,t)$ is denoted by

$$w(x(I), y(J), n\Delta t) = w_{I,J}^n \quad \text{for} \quad \begin{matrix} I, J = 0,1,2,... \\ n = 0,1,2,... \end{matrix}. \tag{20}$$

The wave equation (7) is discretized using a three-level explicit difference scheme:

$$\frac{1}{c_2^2} \frac{w_{I,J}^{n+1} - 2w_{I,J}^n + w_{I,J}^{n-1}}{\Delta t^2} = \frac{w_{I+1,J}^n - 2w_{I,J}^n + w_{I-1,J}^n}{h^2} + \frac{w_{I,J+1}^n - 2w_{I,J}^n + w_{I,J-1}^n}{h^2}. \tag{21}$$

Thus the displacement at time step (n+1) is determined explicitly from the known values at time steps n and (n-1). This scheme is accurate to second order. The boundary condition along $x = 0$ is discretized as follows:

$$w_{0,J}^{n+1} = w_0 f[(n+1)\Delta t] \quad \text{for} \quad J = 0,1,2,... \tag{22}$$

Along the crack line, $y = 0$, $x < l(t)$,

$$w_{I,1}^{n+1} - w_{I,0}^{n+1} = 0 \quad \text{for} \quad I = 0,1,2,..I_{crack}. \tag{23}$$

I_{crack} is the index identifying the current location of the crack tip. For $I > I_{crack}$, the boundary condition is specified through the layer constitutive equation (17) as follows:

$$w_{I,0}^{n+1} = \begin{cases} \dfrac{1}{1+h/d} w_{I,1}^{n+1} & 0 < w_{I,0}^n < \gamma_y d \\ \dfrac{w_{I,1}^{n+1} - h\gamma_y (1 + k_2/k_1)}{1 - (h/d)(k_2/k_1)} & \text{for} \quad \gamma_y d < w_{I,0}^n < \gamma_f d. \\ 0 & w_{I,0}^n > \gamma_f d \end{cases} \tag{24}$$

unless $w_{I,0}^{n+1} < w_{I,0}^{n} < \gamma_f d$, in which case the layer experiences unloading and this behavior is represented by

$$w_{I,0}^{n+1} = \frac{1}{1+(h/d)(k_s/k_1)} w_{I,1}^{n+1}, \tag{25}$$

where k_s is the unloading slope given by

$$k_s = k_1 \left[\frac{\gamma_y d}{w_{I,0}^{n}} \left(1 + \frac{k_2}{k_1} \right) - \frac{k_2}{k_1} \right]. \tag{26}$$

In this case γ_y is reset to $w_{I,0}^{n}$ and reloading will also occur along (25) until $w_{I,0}^{n+1} > \gamma_y d$, when we revert to (24) with the redefined γ_y. Note that $w_{I,1}^{n+1}$ is known from the results at steps n and (n-1); only $w_{I,0}^{n+1}$ needs to be determined from equations (24) or (25) as appropriate. For a crack that grows under monotonic loading, since the layer is broken sequentially, the unloading curve is never attained. However, if we apply arbitrary loading variations, the layer might experience unloading and even crack arrest and this is the reason for inclusion of the damaged unloading behavior for the layer. This completes the finite difference formulation of the anti-plane cohesive model of the dynamic fracture problem. We now turn to the results of a number of simulations aimed at examining the role of the cohesive zone (model of the actual process zone) on the dynamics of crack growth.

5.3. Dynamic Crack Growth Simulations

We shall consider an edge crack of length l_0 in a half-plane as formulated in Section 5.x. The loading on the specimen is taken to be a ramp function:

$$\dot{w}(0,y,t) = \begin{cases} \ddot{w}_0 t & 0 < t < t_0 \\ \ddot{w}_0 t_0 & t > t_0 \end{cases} \tag{27}$$

Where $\ddot{w}_0$ is the acceleration of the edge $x = 0$ and t_0 is the ramp up time. In the discretized version, this becomes

$$w_{0,J}^{n+1} = \begin{cases} w_{0,J}^{n} + \ddot{w}_0 (n+\tfrac{1}{2})\Delta t^2 & 0 < (n+\tfrac{1}{2})\Delta t < t_0 \\ w_{0,J}^{n} + \ddot{w}_0 t_0 \Delta t & (n+1/2)\Delta t > t_0 \end{cases} \qquad J = 0,1,2,.... \tag{28}$$

If the finite difference scheme is implemented with this loading, the complete stress and velocity fields and the evolution of the cohesive zone are determined by time

stepping in increments corresponding to the stability condition (19). We begin with a description of the field quantities $\dot{w}(x,y,t)$, $\sigma_{31}(x,y,t)$ and $\sigma_{32}(x,y,t)$. The time evolution of these quantities is shown through contour plots in Figures 11, 12 and 13 respectively. In addition to the contours, the variation of the particle velocity and stress components along $x = 0$ is also shown; for the stress component $\sigma_{32}(x,y,t)$ this corresponds to the stress generated in the cohesive layer. The propagation of the stress wave and the crack tip, along with its process zone are apparent in these figures. Normalization is such that the wave speed is unity; the stress wave arrives at $x = 1$ at $t = 1$. The initial crack tip is at $x = 0.2$. ($\ddot{w}_0 = 0.01$, $d = 0.01$, $k_1 = 1$, $k_2 = 0.25$, $\gamma_y = 0.02$, $\gamma_f = 0.1$). Thus, the complete dynamic fracture problem is simulated and the resulting stress and displacement fields, along with the development of the crack tip process zone and the growth of the crack are determined through this analysis.

The main result here is simply that a model of the crack tip process zone through a cohesive zone enables a simulation of the crack growth process completely, *without imposing a crack speed as is usually done in analyses.* We shall focus on the cohesive zone model simulation and raise a number of issues that provide insight into the role of the process zone in dynamic fracture. Are there suitable local parameters for the description of this dynamic crack growth process? Does steady-state crack growth occur? Are there universal relations that govern the evolution of the process zone as a function of the speed? This is usually the concept used in applying results from steady-state analysis to other problems. We address these issues below.

5.3.1. Evolution of the crack tip process zone

We begin with the development and growth of the process zone at the crack tip. Along the layer, the point, $x_{le}(t)$, that first reaches γ_y is termed the leading edge of the process zone and the point, $x_{te}(t)$, that first reaches γ_f is termed the trailing edge of the process zone which is the physical crack tip. The initial conditions for the simulation do not include a process zone and hence a process zone first develops at the crack tip as the leading edge of the zone grows out in the x-direction. The trailing edge of the zone is stationary at the initial crack tip until the strain at this point reaches γ_f, after which the trailing edge also grows out in the x-direction. The growth of the leading and trailing edges can be used to determine the speeds of the leading and trailing edges and the size of the cohesive zone; these are shown in Figures 14 and 15 for five simulations corresponding to five different loading rates. The oscillations that appear in the velocity plots are an artifact of differentiating

numerical data and we assume a more refined time stepping process would smooth out the oscillations. Four important observations can be made from these results: first, while the leading edge of the cohesive zone indicates a smooth acceleration, the trailing edge - the physical crack tip - appears to jump to a high velocity rather quickly. This result is in agreement with experimental observations of the crack speed jump at initiation (Ravi-Chandar and Knauss, 1984, Fineberg *et al.*, 1992), but we still need to examine the physical basis in the cohesive zone model for this initial jump in velocity. Second, the size of the cohesive zone, $\alpha(t)$, increases rapidly as the leading edge accelerates from the stationary crack tip; after the trailing edge begins to grow rather abruptly, $\alpha(t)$ decreases rapidly just after initiation and more gradually later. This indicates that the initiation of crack growth (nucleation) is more difficult than continued growth (propagation). This could be due to the fact that our simulation began without an initial process zone; we will explore this further in this paper. Third, the speeds of the leading and trailing edges of the process zone continue to increase at nearly the same rate, while the process zone decreases in size slowly. If the simulation is continued for very long times, the speeds would approach the shear wave speed and the process zone would tend to zero. This is to be expected from the fact that energy is supplied to the layer by shear waves and hence cracks cannot run faster than the energy source. Lastly, the material in the layer is rate independent and hence does not set any limits on the rate of dissipation in the process zone. However, rate dependence is clearly observed both in the initiation and growth of the process zone and in the velocity histories of the leading and trailing edges, providing a possible basis for rate dependent fracture behavior in rate independent materials. We will examine the behavior of the process zone in greater detail in terms of the applied loading.

Having postulated the failure criterion in terms of the critical strain in the layer, the parameter controlling the evolution of fracture process zone and the crack velocity must be the rate at which energy is supplied to the crack tip region, $F(\Gamma)$. This is easily calculated for the cohesive zone model (Freund, 1990) as the rate of work done on the cohesive zone:

$$F(\Gamma) = \int_{x_{te}(t)-x_{le}(t)}^{0} 2\tau_{layer}(\xi,t)\frac{\partial w(\xi,0,t)}{\partial t}d\xi + v(t)\int_{0}^{\gamma_f} 2\tau_{layer}(\gamma)d\gamma, \qquad (29)$$

where $\xi = x - x_{le}(t)$, and $v(t) = \dot{x}_{te}(t)$ is the speed of the trailing edge of the process zone. The right hand side indicates the rate at which the crack tip process zone can

dissipate energy. The integral in the second term is the work of separation determined by the layer constitutive model, Γ_s. The first term is caused by time rate of change of displacements within the cohesive zone as well as the changes in the cohesive zone size itself - this is the nonsteady-state term; its magnitude depends on the particle velocity which in turn depends on the loading rate thereby introducing rate dependence in the crack growth behavior. For crack initiation, the second term is zero, but the first term (with $x_{te}(t) = l_0$) describes the rate of dissipation in developing the process zone and clearly this is rate dependent, even though the material model is completely rate independent. The variation of the energy flux from the five simulations corresponding to Figure 14 is shown in Figure 16; also marked on this figure by the dotted line is the energy flux at the instant of trailing edge initiation. Rate dependence of the evolution of the fracture process zone is evident. We can now interpret the variations in the speeds and process zone size in terms of the energy supply rate.

The energy flux into the crack tip region is typically used as the controlling input parameter but this quantity is determined not only by the applied loading, but also by the development of the process zone; that is, the capacity of the crack tip to absorb power is dependent on the rate of evolution of the process zone. In other words, this energy flux is not a controlling parameter, but is itself determined by the response of the crack tip. Thus, we can consider the results plotted in Figures 17, and 18 as a phase-space representation of the growth of the cohesive zone. Figure 17 shows the variation of the speed of the trailing edge with the energy flux or equivalently the dissipation rate. Figure 18 shows the variation of the process zone size $\alpha(t)$ with the dissipation rate. There is some numerical scatter in the results, particularly since the speeds are derived quantities, but the general trend is clear. Some observations from these plots: first, there appears to be an attractor; all simulations appear to tend towards a particular curve. In Figure 17, this would be the line $\dot{D}(t) = \Gamma_s v_{te}(t)$. But from (29) this is the rate of dissipation for a crack moving at a steady-state speed $v_{te}(t)$. Corresponding to this steady-state crack growth, the process zone size decreases again following the same curve in all the simulations. Thus, we can define steady-state as that state for which

$$\dot{D}(t) = \Gamma_s v_{te}(t), \tag{30}$$

and

$$\alpha(t) = X(v_{te}(t)). \tag{31}$$

Freund and Douglas (1982) considered the plastic zone near the tip of a crack propagating at a constant speed under small-scale yielding in mode-III, with an elastic-plastic constitutive model. Using a critical strain criterion, they derived the variation of the size of the plastic zone in a form similar to (31). Since their results are derived from decoupling the fracture criterion from the stress analysis, it appears that under the steady-state conditions defined above, the motion of the crack with varying speed can be considered to be a succession of changes through steady-states at different speeds; in other words, for the case of steady-state crack growth, the failure criterion could be decoupled from the governing equations within the context of a cohesive zone model; this idea was used by Freund (1972) in examining non-uniform crack growth in elastic materials.

Secondly, non-steady-state paths are permissible in this process zone model and, indeed, the initiation of process zone and crack growth are definitely non-steady-state processes as can be seen from Figures 17, and 18. This is most easily seen in Figure 18; while steady-state conditions require a fixed α at a fixed dissipation rate, clearly during the initial evolution of the process zone, the size of the process zone and the dissipation rate depend on the rate of loading. During this non-steady growth of the process zone, the trailing edge is stationary; as the process zone evolution approaches the path corresponding to steady-state evolution, the dissipation rate corresponding to steady-state cannot be sustained unless the trailing edge also initiates and grows at a speed corresponding to steady state crack growth; thus, the trailing edge initiates and jumps to the speed appropriate to steady-state growth at this dissipation rate, as indicated in Figure 17. We now have two branches in the $\dot{D}$ vs v_{te} plot: there exists a steady-state branch given by equation (30). Even in the absence of a cohesive zone model, one could construct this branch. There is the possible state that $v_{te} = 0$ for all $\dot{D}$; that is, the physical crack remains stationary while dissipation occurs elsewhere in the process zone and we will refer to this as the stationary branch. When the secondary dissipation process (growth of the process zone) is no longer able to accommodate the energy flux from the loading, the only possibility provided in this cohesive model is for the trailing edge speed to jump from the stationary branch to the steady-state branch. Note that we have avoided describing the loading on the crack in terms of local parameters such as the dynamic stress intensity factor or the dynamic energy release rate per unit crack

advance. These turn out to be unnecessary; the dynamic stress intensity factor is only a reinterpretation of the wave loading and therefore not needed in a full field simulation. The dynamic energy release rate per unit crack advance must always equal Γ_s in this rate independent model and hence is nor a useful parameter in defining the dynamic crack growth criterion; hence, only the energy flux rate is important in establishing the growth of the process zone and crack tip.

We now have a complete description of the growth of a crack due to dynamic loading, within the context of a cohesive zone model. Given the loading, geometry and the cohesive zone properties, we are able to calculate completely the evolution and growth of the process zone and the crack tip. An important observation from this set of simulations is that in this cohesive zone model, all cracks quickly approach the steady-state and remain in that state. This, however, is not always the case. We have imposed a severe constraint in the model that the process zone can only expand in length and not in thickness. Real cracks may, and often do, find this other mechanism of power consumption during crack growth and if we allow for this possibility, non-steady-state paths can be sustained.

6. CONCLUSION

With a view toward establishing a nondestructive procedure for evaluation of the impact properties of polycarbonate windshield material, we have set up the following experiments (i) a split-Hopkinson bar apparatus for impact strength measurement, (ii) an instrumented impact tester for impact toughness measurement and (iii) a monochromator with a birefringence measuring Babinet-Soleil compensator for optical characterization. Some polycarbonate specimens have been identified as potential candidates for evaluation of the proposed method.

A dynamic crack growth model based on an extension of the Dugdale-Barenblatt has been formulated and solved through a finite difference scheme. This model exhibits many of the features observed in dynamic fracture experiments.

REFERENCES

Achenbach, J.D. and Dunayevsky, V. (1981), Fields near a rapidly propagating crack in an elastic-perfectly plastic material, *Journal of the Mechanics and Physics of Solids*, **29**, pp.283-303.

Anderson, H. and Bergkvist, H. (1970), Analysis of a non-linear crack model, Journal of the Mechanics and Physics of Solids, **18**, pp.1-28

Carpinteri, A. (1994), Cracking of strain-softening materials, in **Static and Dynamic Fracture Mechanics**, edited by Aliabadi, M.H. Brebbia, C.A. and Parton V.Z. Computational Mechanics Publications Inc.

Davis, A. and Sims, D. **Weathering of Polymers**, Applied Science Publishers, London, 1983, p.153.

Fineberg, J. Gross, S.P. Marder, M. and Swinney, H.L. (1991), Instability in dynamic fracture, *Physical Review Letters, 67*, p.457.

Freund, L.B. and Douglas, A.S. (1982), The influence of inertia on elastic-plastic antiplane shear crack growth, *Journal of the Mechanics and Physics of Solids*, **30**, pp.59-74.

Freund, L.B. (1990), **Dynamic Fracture Mechanics**, Cambridge University Press, Cambridge

Johson, E. (1992), Process region changes for rapidly propagating cracks, *International Journal of Fracture*, **55**, pp.47-63.

Kalthoff, J.F. (1983), On some current problems in experimental fracture dynamics, Workshop on Dynamic Fracture, edited by W.G. Knauss, K. Ravi-Chandar and A.J. Rosakis, California Institute of Technology, Pasadena, pp.11-35.

Kobayashi, A.S. and Mall, S, (1978), Dynamic fracture toughness of Homalite-100, *Experimental Mechanics*, **18**, pp.11-18.

Kostrov, B.V. (1966) Unsteady propagation of longitudinal shear cracks. *Applied Mathematics and Mechanics*, **30**, pp.1241-1248.

Ravi-Chandar, K. and Knauss, W.G. (1984a) An experimental investigation into dynamic fracture: I. Crack initiation and crack arrest, *International Journal of Fracture*, **25**, pp.247-262.

Ravi-Chandar, K. and Knauss, W.G. (1984b) An experimental investigation into dynamic fracture: II. Microstructural aspects, *International Journal of Fracture*, **26**, pp.65-80.

Ravi-Chandar, K. and Knauss, W.G. (1984c) An experimental investigation into dynamic fracture: III. On steady state crack propagation and crack branching, *International Journal of Fracture*, **26**, pp.141-154.

Ravi-Chandar, K. and Knauss, W.G. (1984d) An experimental investigation into dynamic fracture: IV. On the interaaction of stress waves with propagating cracks, *International Journal of Fracture*, **26**, pp.189-200.

Ravi-Chandar, K. and Yang, B. (1995) Dynamic fracture of brittle materials, submitted, *Journal of the Mechanics and Physics of Solids*, August 1995.

Slepyan, L.I. (1976), Crack dynamics in an elastic-plastic body, *Mechanics of Solids (Meckanika Tverdogo Tela)*, **11**, pp.126-134.

Sullivan, T.O. (1982), The propagation and arrest of an edge crack in an elastic half-space under conditions of anti-plane shear: Analytical and numerical results, Ph.D. Thesis, California Institute of Technology, Pasadena.

Treloar, L.R.G. **Physics of Rubber Elasticity**, Oxford University Press, 1949, p.129.

Ungsuwarangsri, T. and Knauss, W.G. (1987), The role of damage softened material behavior in the fracture of composites and adhesives, International Journal of Fracture, **35**, pp.221-241.

Van Krevelen, D.W. **Properties of Polymers**, Elsevier, Amsterdam, 1990, p.298.

West, B.S. "Development of bird impact resistant crew enclosures for aircraft", in Structural Impact and Crashworthiness, Vol2. ed. J. Morton, Elsevier, London 1984, pp. 696-709.

Xu, X.-P. and Needleman, A. (1994), Numerical simulations of fast crack growth in brittle solids, Journal of the Mechanics and Physics of Solids, **42**, pp.1397-1434.

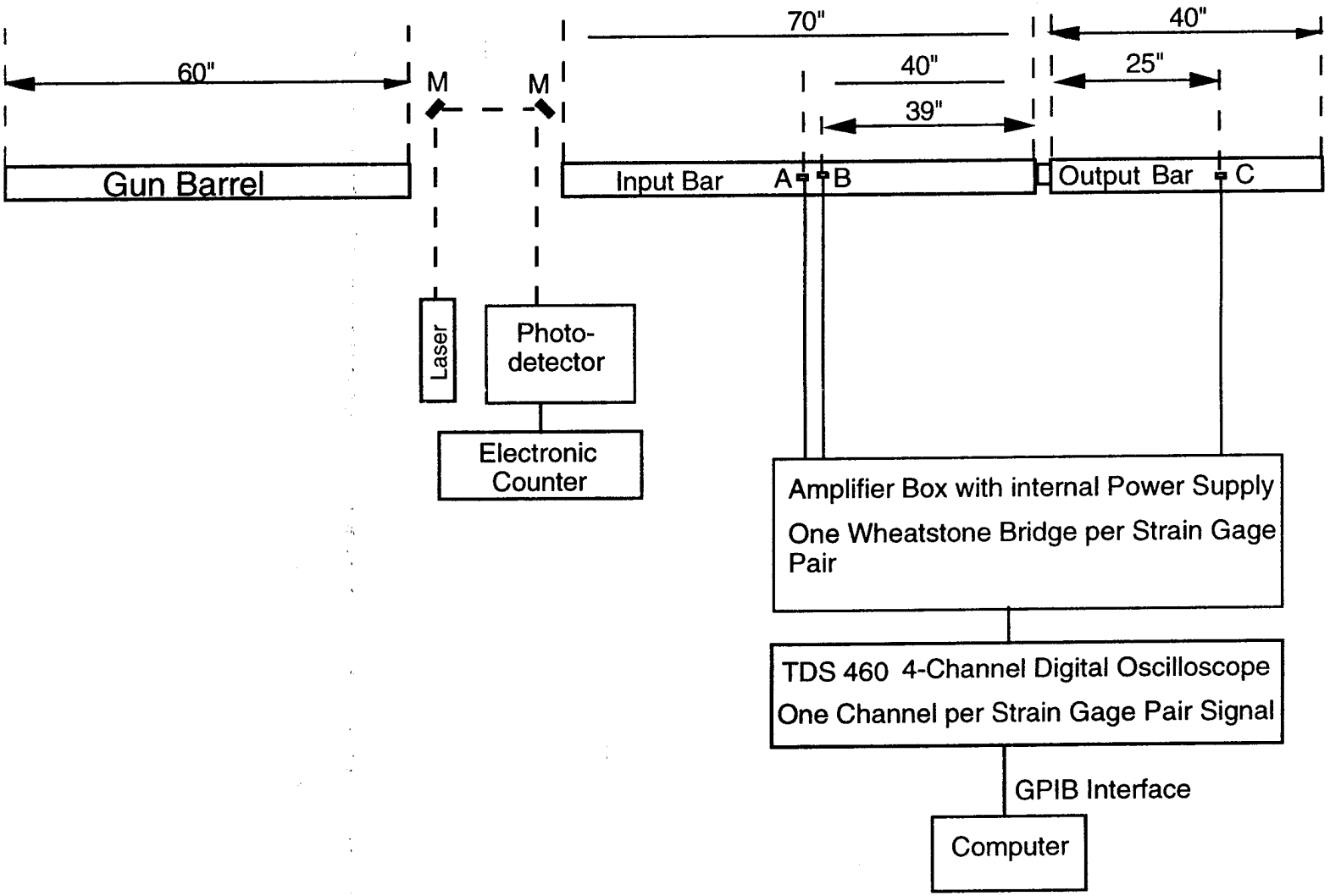

Figure 1. Experimental arrangement of the split Hopkinson pressure bar.

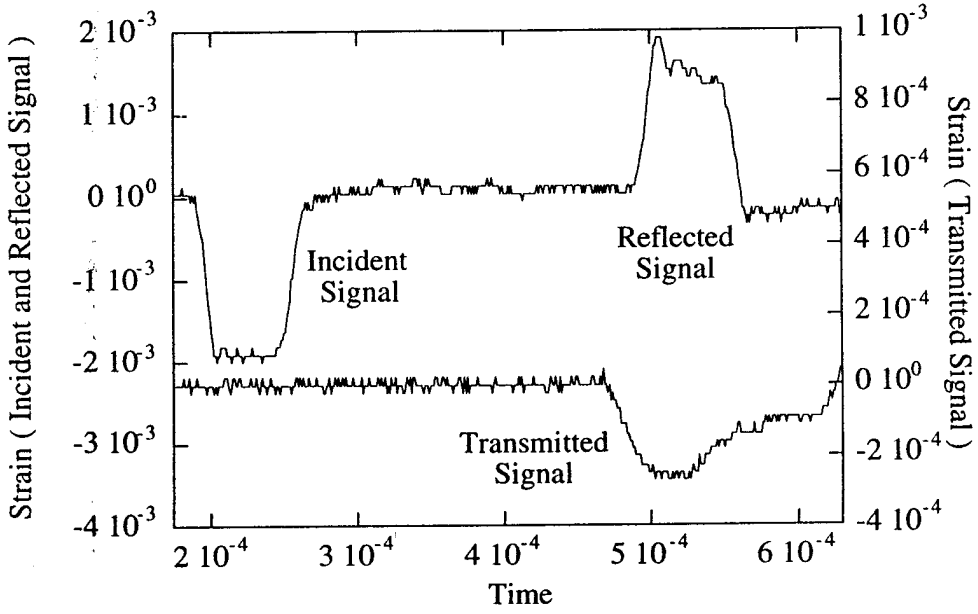

Fig. 2 : Typical strain gage signal traces measured in the input and output bar strain gages.

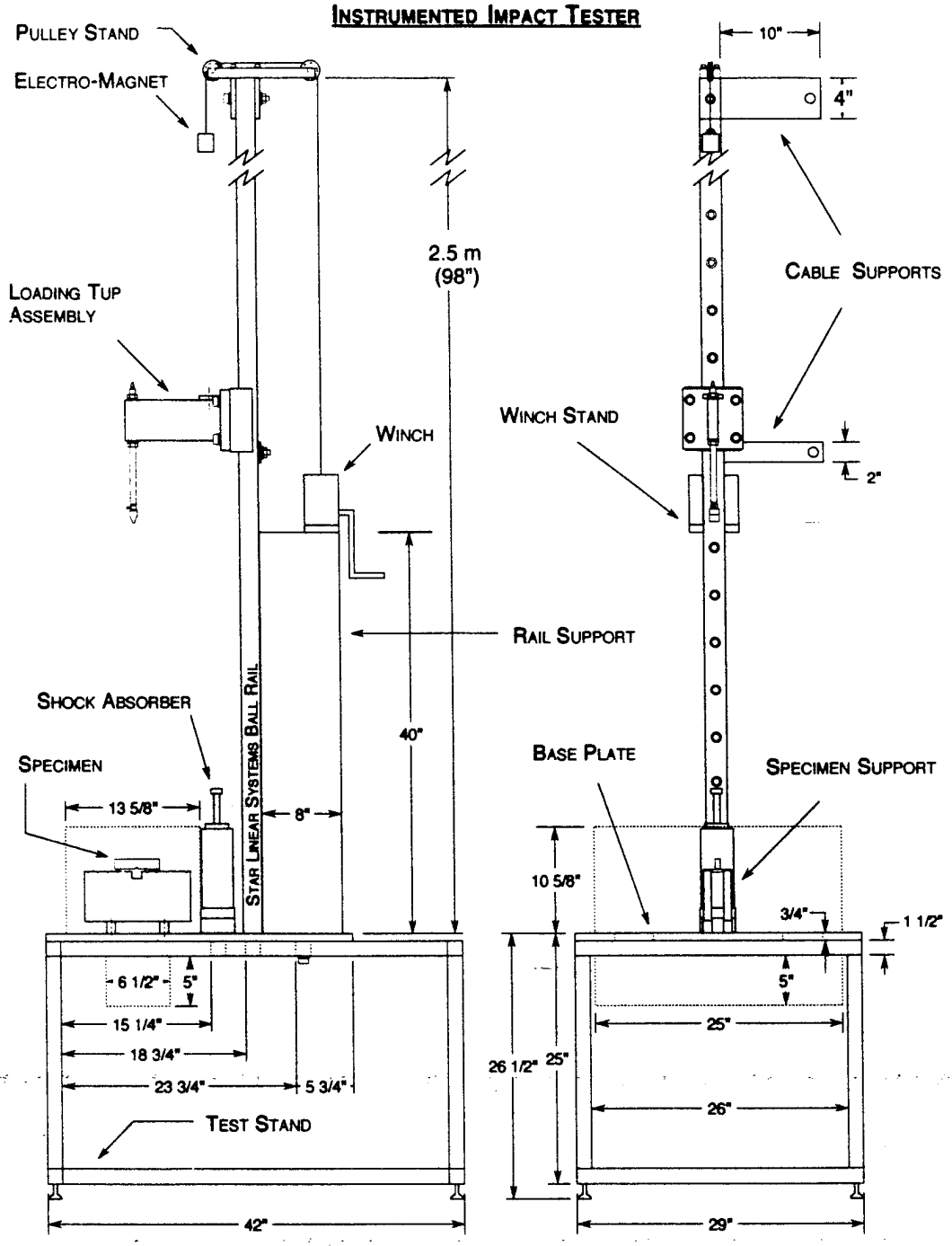

Figure 3. Instrumented impact tester.

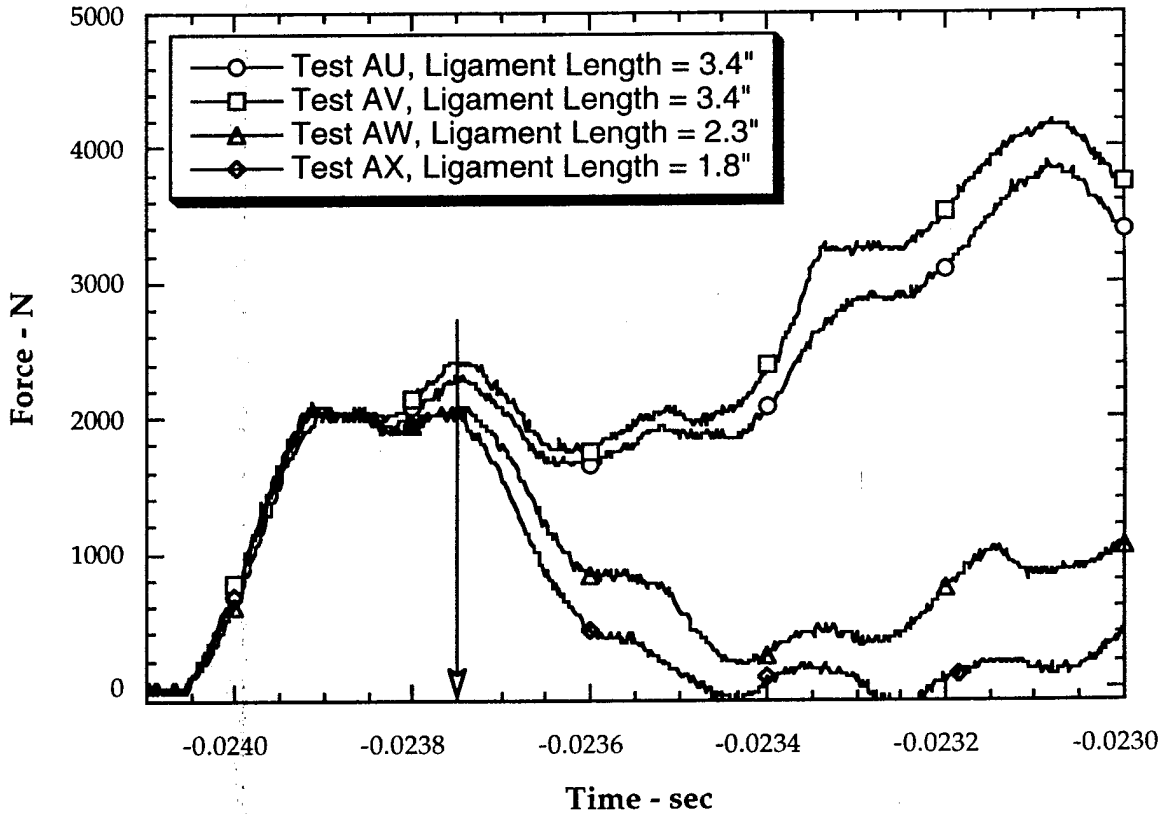

Figure 4. Force transducer output from four different specimens using the instrumented impact tester.

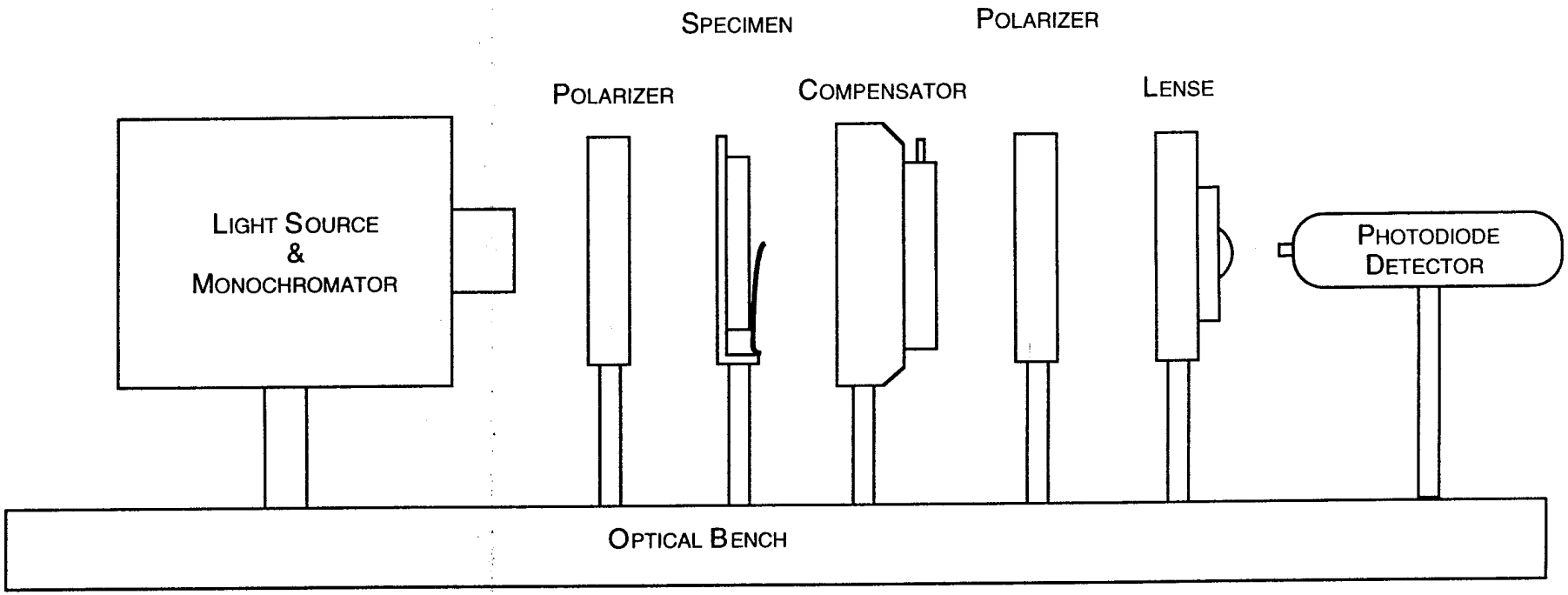

Figure 5. Monochromator and birefringence measurement apparatus.

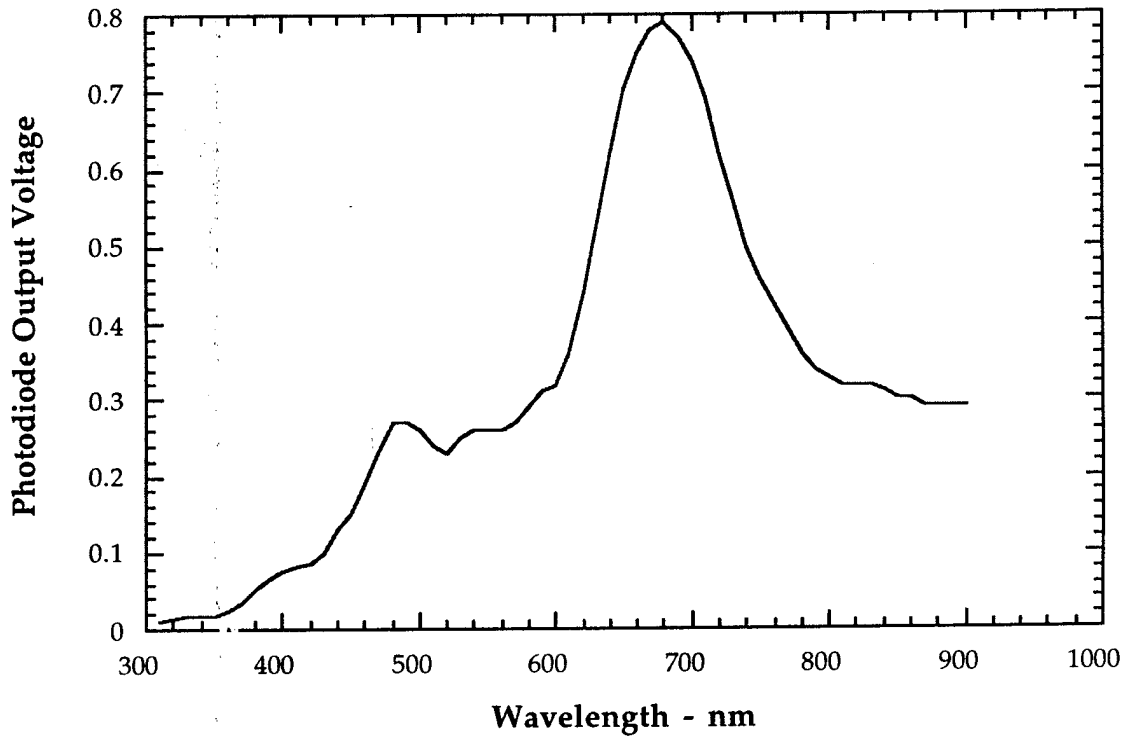

Figure 6. Spectral output of the light source and detector response.

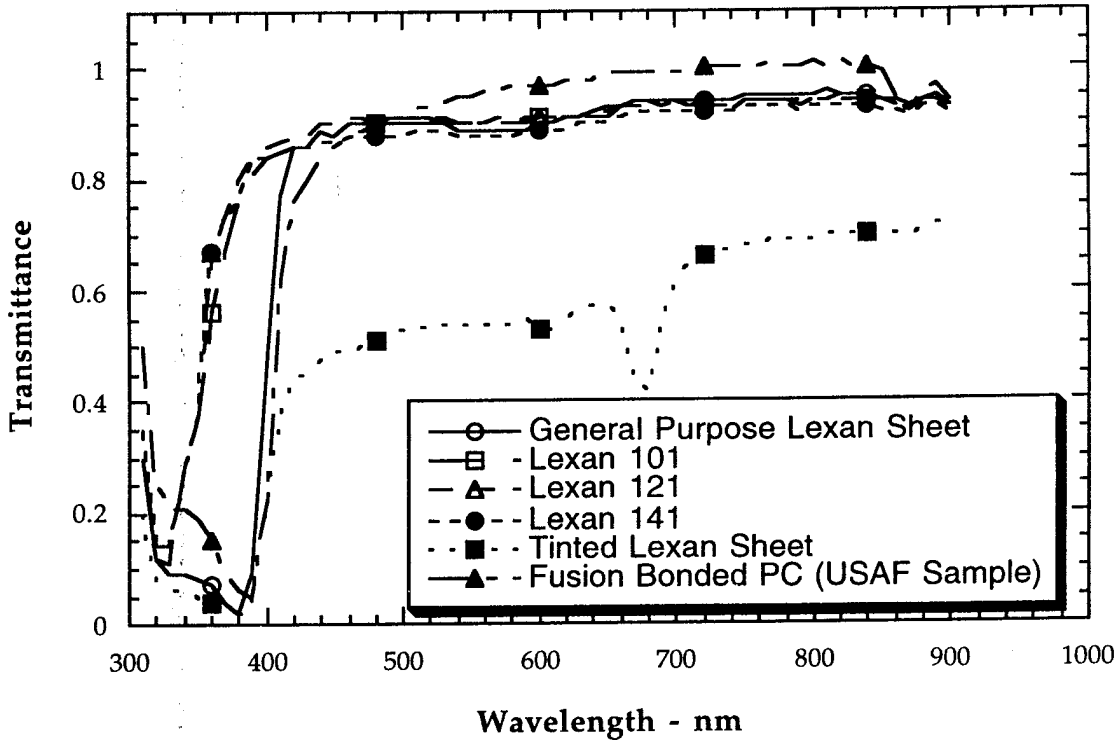

Figure 7. Spectral tranmittance of six different grades of polycarbonate.

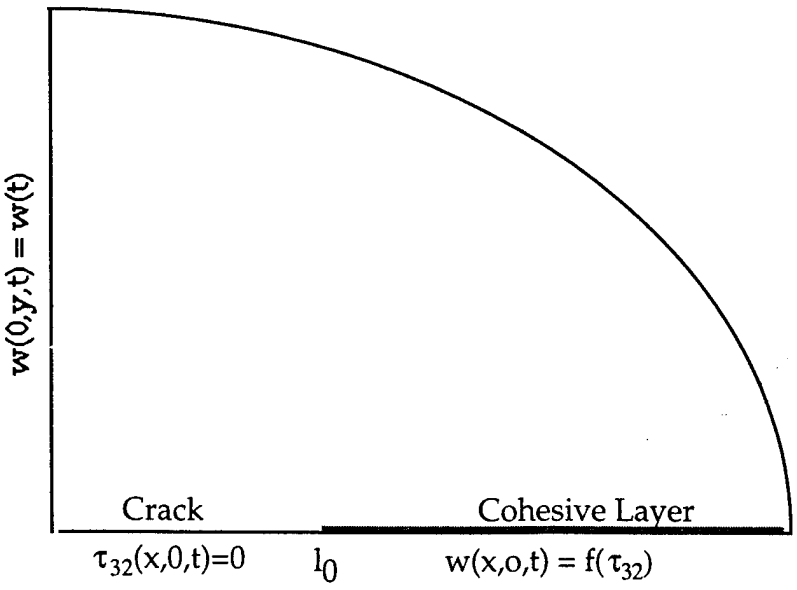

Figure 8. Geometry of the edge crack in a half-space under anti-plane shear with a cohesive layer material ahead of the crack tip, along the line $y = 0$.

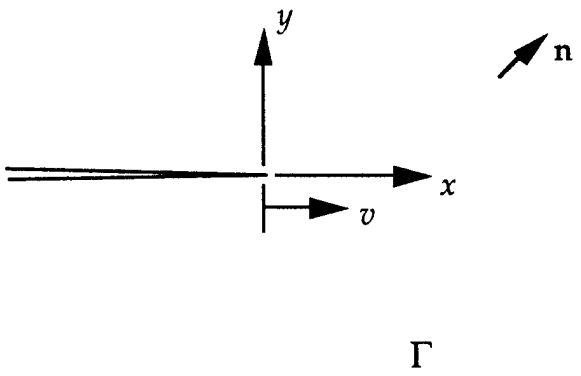

Figure 9. Contour used for the calculation of the energy flux integral.

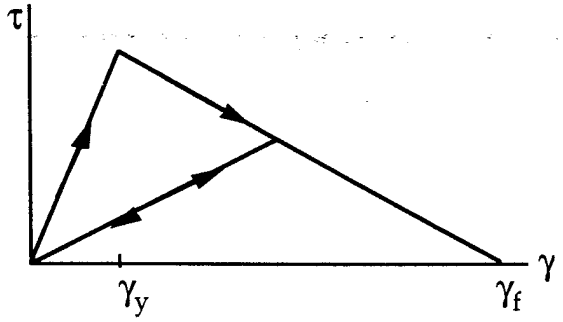

Figure 10. Idealized constitutive behavior of the cohesive layer material; the initial stiffness is taken to be identical to that of the bulk material.

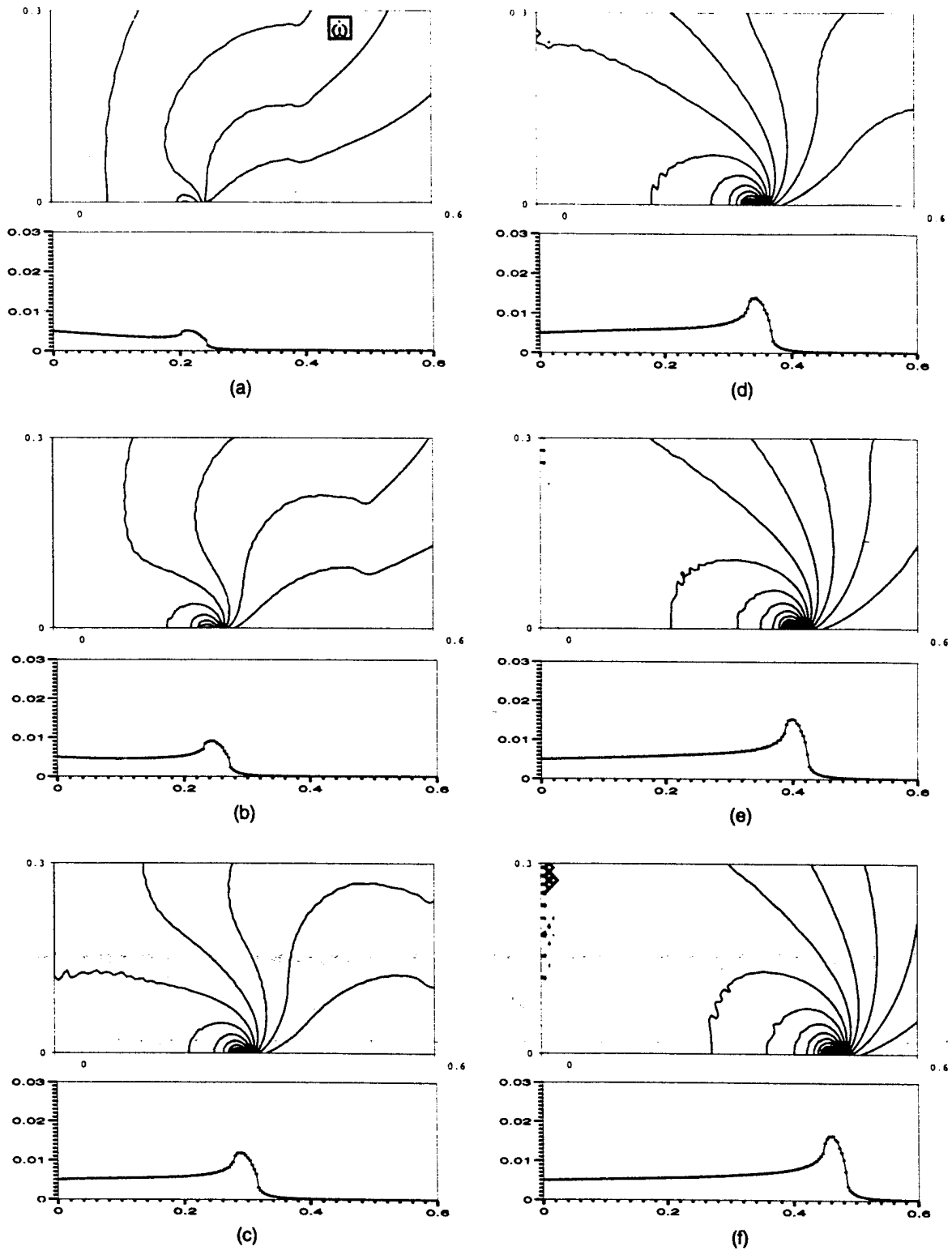

Figure 11. Contour plots of $\dot{w}(x,y,t)$ at selected times; also shown is the value along the line $y = 0$. (a) t = 0.9, (b) t = 1.0, (c) t = 1.1, (d) t = 1.2, (e) t = 1.3 and (f) t = 1.4.

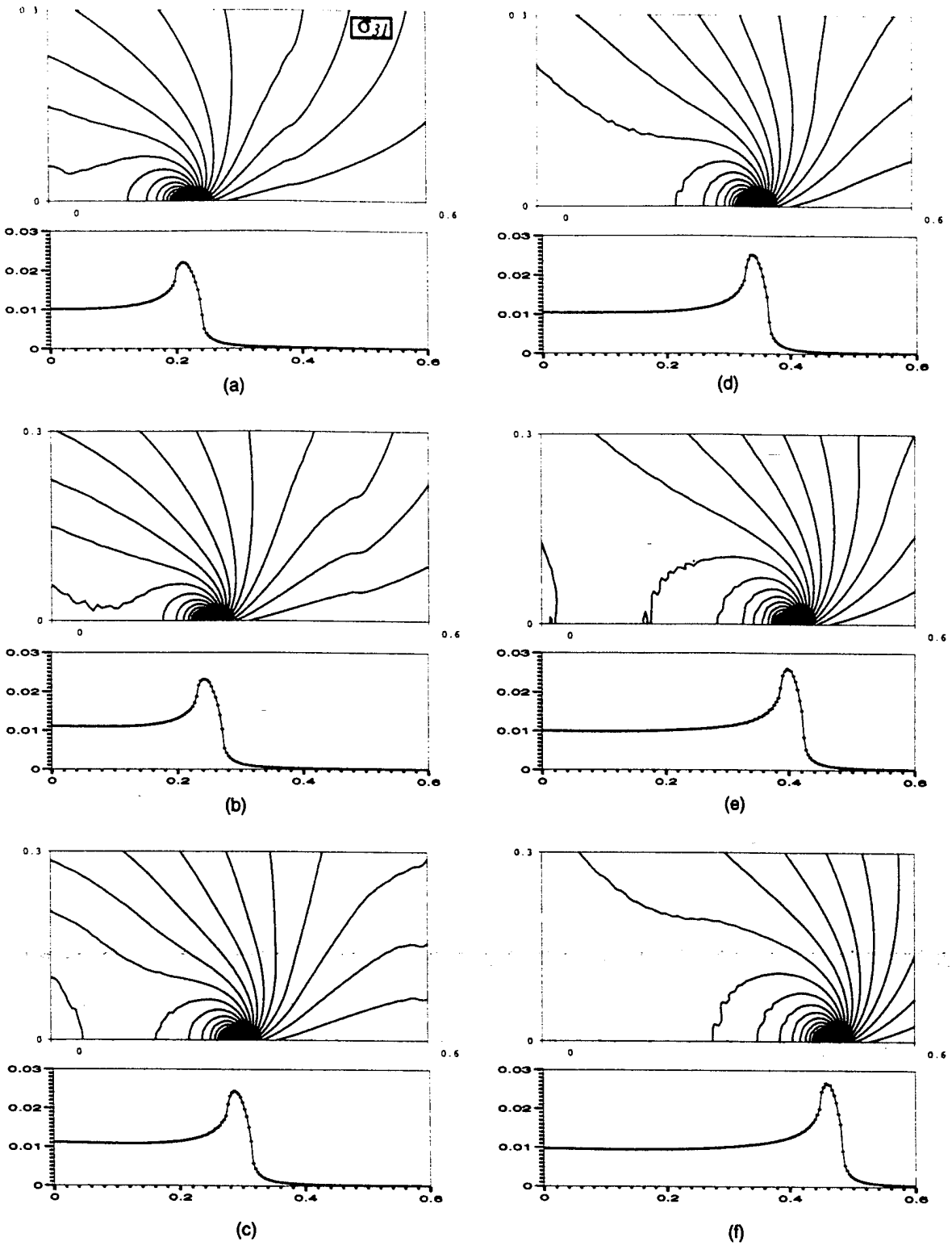

Figure 12. Contour plots of $\sigma_{31}(x,y,t)$ at selected times; also shown is the value along the line $y = 0$. (a) t = 0.9, (b) t = 1.0, (c) t = 1.1, (d) t = 1.2, (e) t = 1.3 and (f) t = 1.4.

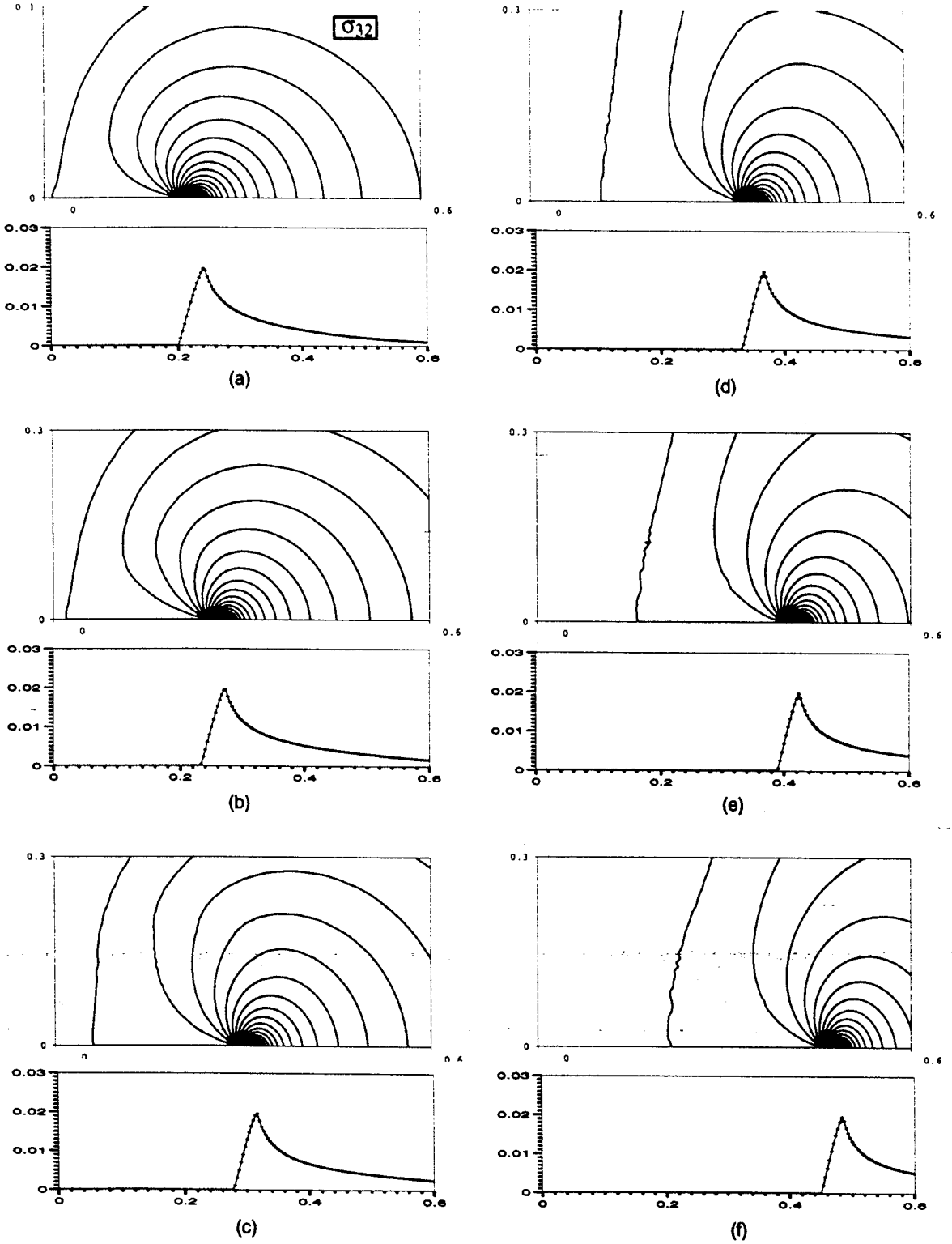

Figure 13. Contour plots of $\sigma_{32}(x,y,t)$ at selected times; also shown is the value along the line $y = 0$. (a) t = 0.9, (b) t = 1.0, (c) t = 1.1, (d) t = 1.2, (e) t = 1.3 and (f) t = 1.4.

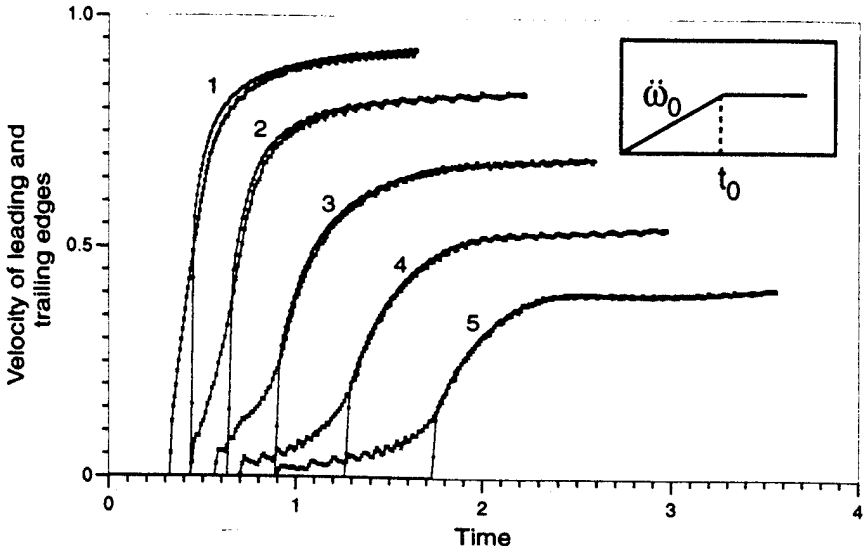

Figure 14. Growth of the leading and trailing edges of the cohesive zone. Results from five simulations at increasing load levels are shown. The rist time was held constant at t0 = 0.5; the acceleration was varied such that = (1) 0.03, (2) 0.01, (3) 0.005, (4)0.003 and (5) 0.002 in the five simulations.

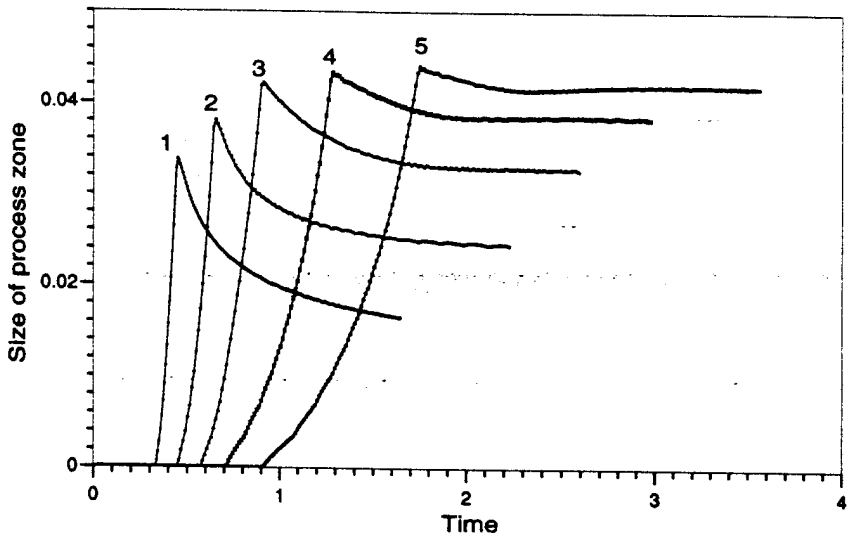

Figure 15. Evolution of the process zone size with time. Results from five simulations corresponding to that shown in Figure 14 are shown.

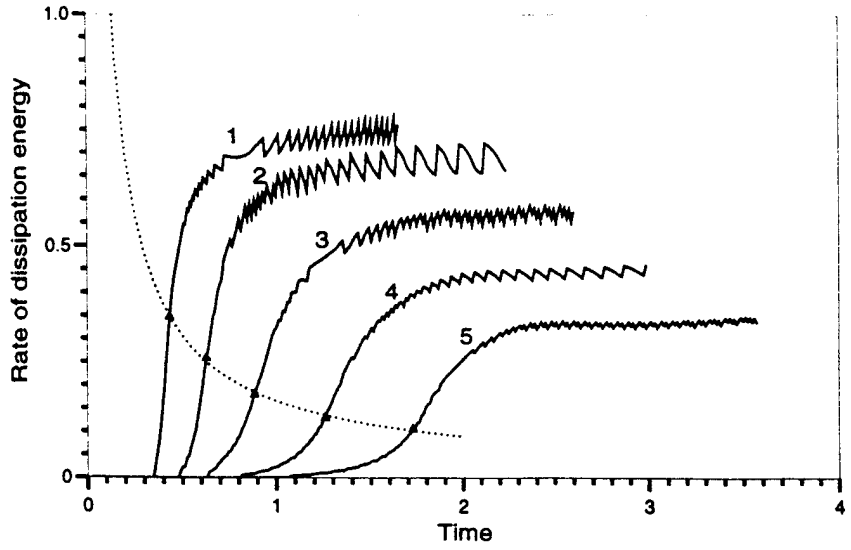

Figure 16. Normalized rate of dissipation energy in the process one as a function of time; the onset of crack growth is identified by the points. The rate dependence of the initiation is evident.

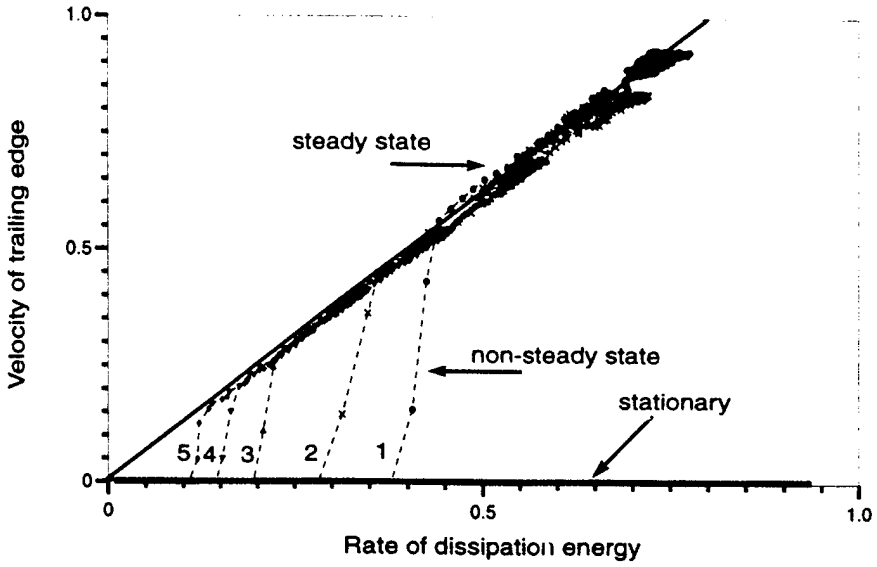

Figure 17. Variation of the trailing edge velocity with the normalixed dissipation rate.

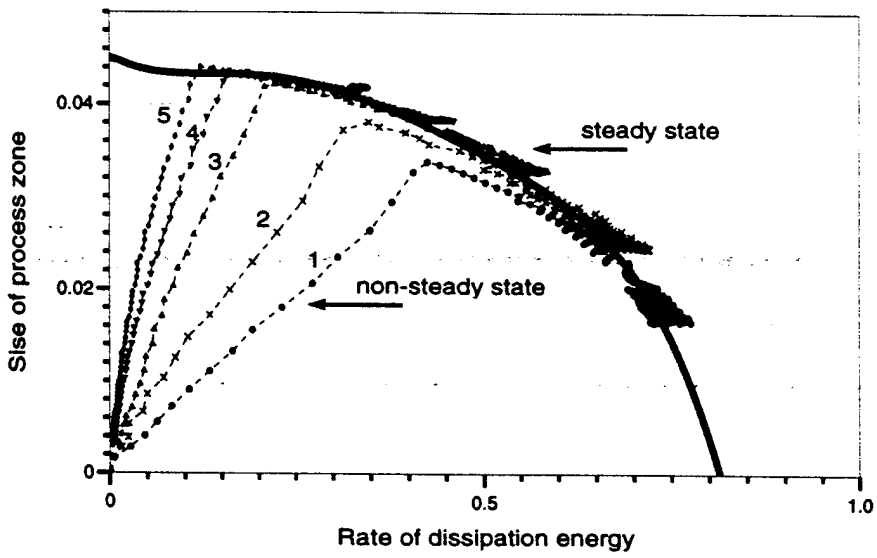

Figure 18. Variation of the size of the process zone with normalized dissipation rate.